Journal Pre-proof

Generation and properties analysis of 3D mesoscale models for plain and fiber reinforced concretes

Chaohui Zhang, Peng Liu, Kai Li, Caijun Shi

PII: S0958-9465(20)30221-3

DOI: https://doi.org/10.1016/j.cemconcomp.2020.103714

Reference: CECO 103714

To appear in: *Cement and Concrete Composites*

Received Date: 27 March 2020

Revised Date: 10 June 2020

Accepted Date: 15 June 2020

Generation and properties analysis of 3D mesoscale models for plain and fiber reinforced concretes

Chaohui Zhang[1], Peng Liu[2], Kai Li[1*], Caijun Shi[1*]

[1] *Key Laboratory for Green & Advanced Civil Engineering Materials and Application Technology of Hunan Province, International Innovation Center for Green & Advanced Civil Engineering Materials of Hunan Province, College of Civil Engineering, Hunan University, Changsha 410082, China*

[2] *College of Mechanical and Vehicle Engineering, Hunan University, Changsha 410082, China*

Abstract: Model construction is a key and indispensable step to understand the internal structure of concrete at the micro-/mesoscale level, which affects its properties in practice. In this paper, a practical and applicable method is proposed for generating the mesoscale structure of plain and fiber reinforced concretes. In this method, cell fracture algorithm was developed to obtain arbitrary-shaped aggregates, Surface subdivision (Catmull–Clark subdivision algorithm), Displacement mapping and Laplace smoothing algorithm were developed to constructed rough surface of realistic aggregates. Random algorithm was used to generate fibers, the interactions between aggregates and fibers were detected and solved by collision algorithm. The influence of shape, size and volume fractions of aggregate, together with fiber's orientation on the structure and properties of plain and fiber reinforced concrete were studied. Compared with experimental data and previous works, the proposed models can well predict the volume fraction of the interfacial transition zone (ITZ) and the elastic modulus of plain and fiber reinforced concretes. This paper provides a promising tool for numerical and analytical research of plain and fiber reinforced concretes.

Keywords: Mesoscale model; Concrete; Fiber reinforced concrete; Interfacial transition zone; Elastic modulus

*Corresponding author: cshi@hnu.edu.cn (Caijun Shi); kaili@hnu.edu.cn (Kai Li)

1. Introduction

Concrete is a multi-phase and heterogeneous material. It consists of three important components: cement paste, aggregate and the interfacial transition zone (ITZ). Fiber is often added into concrete in practice to improve its mechanical performance, including the flexible strength, toughness, etc. [1]. At mesoscale, fiber-reinforced concrete (FRC) can be simplified as aggregates and fibers embedded in the cement matrix, whereas the ITZ is the interface between different phases. Still, it is very difficult to precisely understand the realistic structure of plain and fiber-reinforced concretes by traditional experimental methods without destroying their structures. X-ray tomography image-based reconstruction technique [2, 3] is a promising approach to solve this problem, however, this new technique requires specialized instruments and is time-consuming, laborious and thus expensive. Moreover, the resolution of this approach has an important effect on the accuracy of the obtained results, which limits its application in cementitious materials. As an alternative, numerical modeling provides an economic and reliable way to construct the concrete structure at mesoscale.

Various mesoscale models for simulating concrete structures have been developed in recent decades. Aggregate generation technologies, such as Euclidean geometry [4, 5], low polyhedral [6, 7] and sphere harmonic function [8], have made remarkable progress. Aggregates are generally treated as spherical particle [9, 10], so that complex overlapping detection algorithms can be avoided. Besides, aggregates with regular shapes (*i.e.*, Euclidean geometric polyhedron and ellipsoid) are also used to construct the structural model so that the elastic modulus [11], effective diffusion [12], tensile strength [13] and damage behavior [14] of concrete can be studied. Low polyhedral aggregates were developed to model the static [15] and dynamic [6] behaviors of concrete under various loading conditions, which can be generated by mathematical functions on the basis of ellipsoidal particles [16]. Voronoi tessellation method [17] can also be employed to generate such aggregates. In addition, a “taking” and “placing” method was developed to randomly generate 2D non-convex aggregates [18]. Although random sequential addition (RSA) [19] is a common method to model the packing of non-spherical aggregates, discrete element method (DEM) [20-22] has been proven to yield more realistic concrete structures since the contacts between particles are well considered in DEM. Realistic aggregates are generally generated by sphere harmonic function [8, 23], which can be utilized to investigate the fracture behavior of cementitious materials [24] at different scales. Moreover, a method [25] that combines digital image processing, spectral representation and point cloud, was proposed to model 2D and 3D concrete aggregates of arbitrary shapes. X-ray image analysis is able to obtain the real aggregates by scanning the sample's surface. However, the surface fine texture characteristics of aggregates are ignored. For the generation of aggregate, CT scanning technology can only obtain limited and specific aggregates, while numerical model can study a large number of aggregates with different characteristic.

For the generation of randomly distributed fibers, Guan *et al.* [26] assumed that the shape of fiber is ellipsoid, such that the complex embedding detection between fibers can be avoided. However, elliptical fibers are rarely used in engineering. Liang *et al.* [27] used Rand function in MATLAB to generate fibers with different length, but still the interactions between fibers are not well considered. Xu *et al.* [28] proposed a 2D mesoscale model that is able to take both aggregates and fibers into account. Unfortunately, only a limited amount of fibers can be considered in the abovementioned mesoscale models. It is thus quite important to establish the mesoscale model of plain and fiber reinforced concrete with realistic aggregates and fibers, which can be used to predict the volume fraction of ITZs, elastic modulus and mechanical performance of concrete [29].

Calculating the volume fraction of ITZ in concrete by experiments is very difficult, and numerical models seem to be a possible tool. Han *et al.* [30] proposed an one-point probability function, in which the contraction factor (CF) is employed to generate 2D non-convex aggregate, so that the volume fraction of ITZs can be determined by Monte Carlo approach [31, 32]. It is found that the volume fraction of ITZ goes up linearly with the increase of aggregate content. However, 2D models are unable to fully reflect the volume fraction of ITZ in real concrete and 3D models are still required. As for the study on the elastic modulus of concrete, Wriggers *et al.* [5] proposed a mesoscale model but it is only based on spherical aggregates. Gal *et al.* [29] studied the effective elastic modulus of FRC consisting of spherical aggregates and straight fibers, and pointed out that there exists an overestimation of the obtained elastic modulus at the increased volume fraction of fibers. Xu *et al.* [33] derived a Hashin-Shtrikman (HS) model [34] and calculated the effective elastic modulus of three-phase composite materials. It is observed that the effective elastic modulus of composites goes up with the increase of the interfacial elastic modulus, but decreases at the increased thickness of ITZ [35]. Unfortunately, spherical and regular shape of aggregate cannot reflect the real situation in practice.

This paper proposed an economical, effective and reliable method for the generation of plain and fiber reinforced concrete at the mesoscale level. The rough surface texture of realistic aggregate and different fibers are both taken into account. The applications of proposed mesoscale model on the prediction of the ITZ volume fraction and the elastic modulus of plain and fiber reinforced concrete are also included. This work is useful in the field of cementitious materials and can be further used to study the mechanical performance of plain and fiber reinforced concrete in combination with other numerical methods, such as FEM, DEM, etc.

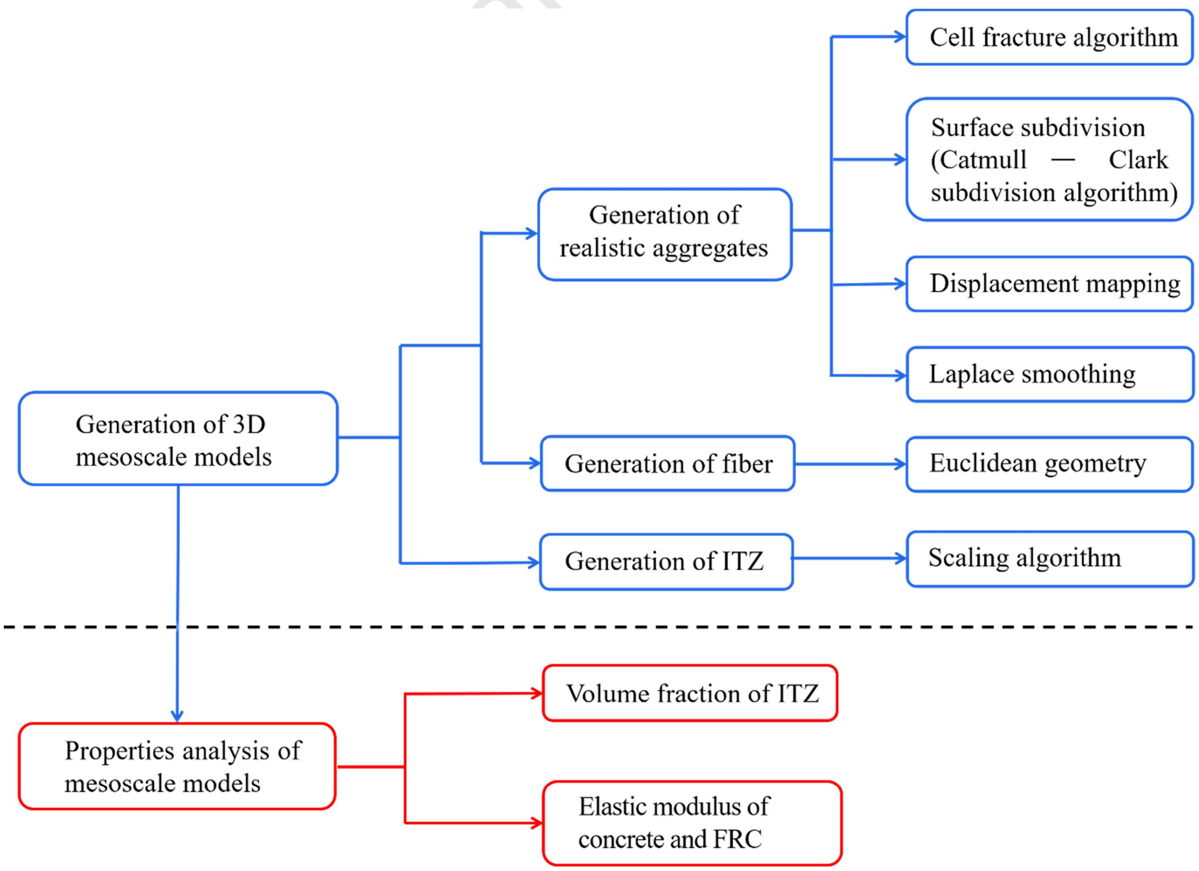

Fig. 1 Framework of this research

2. Generation of 3D mesoscale models for plain and fiber reinforced concretes

2. 1 A new framework of generation of realistic aggregate with rough surface texture

A new framework of generation of realistic aggregate with rough surface texture is proposed in this work, which consists of four main algorithms: (1) Cell fracture; (2) Surface subdivision (Catmull–Clark subdivision algorithm [36]); (3) Displacement mapping; (4) Laplace smoothing.

2.1.1 Cell Fracture

To obtain the realistic aggregate with rough surface texture, the first step is to generate low-polygon aggregates by cell fracture algorithm. An illustration about cell fracture algorithm is shown in Fig. 2. First, random seed points or Voronoi diagrams are generated according to the scatter algorithm [37]. Then, the Voronoi diagrams are separated by Delaunay triangulation algorithm, which divide a region into discrete triangular area [17]. Next, fragments are modeled by filling surface. At last, all the Voronoi diagrams meshes are defined as rigid bodies and expanded in a real-time simulation. In this way, low-polyhedral aggregates of different sizes can be obtained, as indicated in Fig. 3. All simulations are implemented by using Python code.

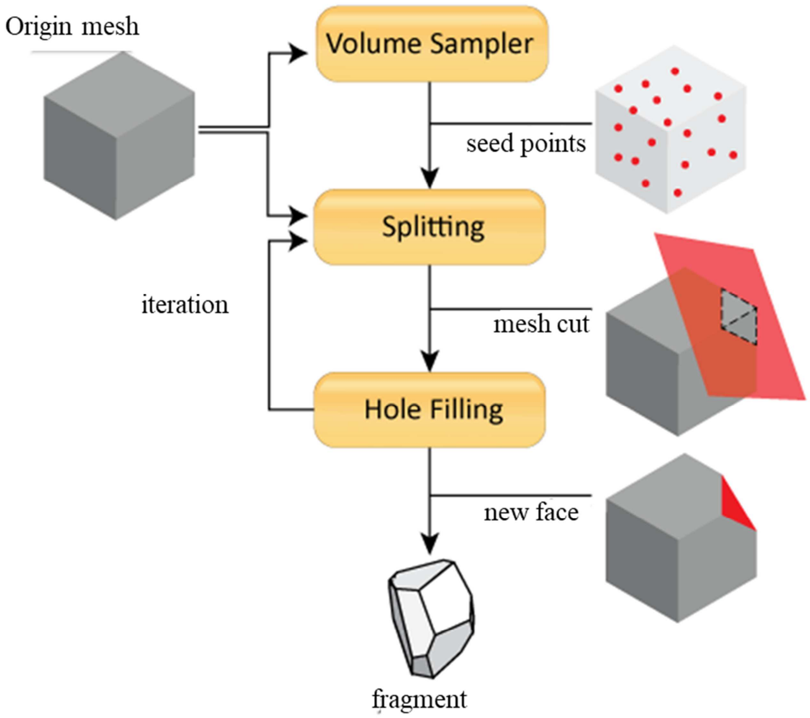

Fig. 2 Schematic diagram of cell fracture algorithm [22]

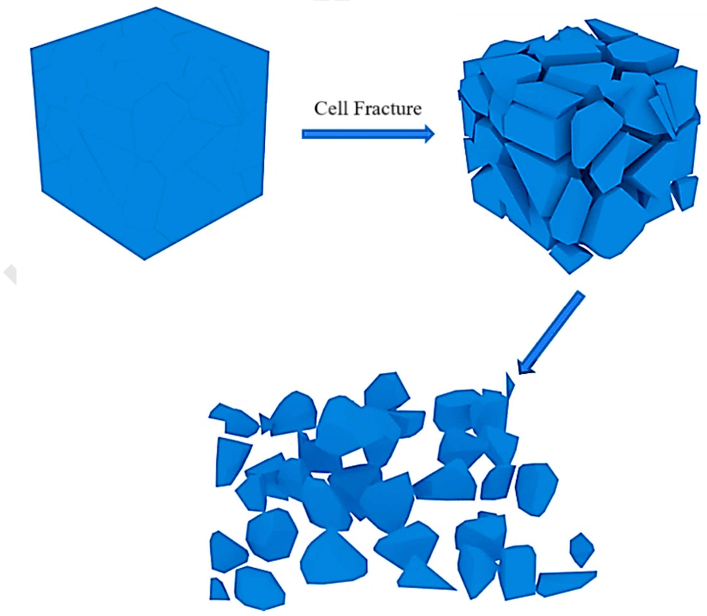

Fig. 3 Generation of low-polygon aggregates by cell fracture algorithm

2.1.2 Surface subdivision

Aggregates generated by cell fracture algorithm are usually of convex shapes. In order to obtain non-convex aggregates, weight function was used to regenerate the coordinates of aggregates:

$$P_i'(x,y,z) = P_i(x,y,z) + \left[f_1(w_{ix}) \quad f_2(w_{iy}) \quad f_3(w_{iz}) \right] P_i(x,y,z) \tag{1}$$

Where, $\widetilde{P}_i(x,y,z)$ and $P_i(x,y,z)$ are the *i*-th initial and updated coordinates of aggregate, respectively. f_1, f_2, f_3 are the weight function, which can be expressed by a constant or random function. Delaunay triangulation algorithm is used to reconstruct the meshes of aggregate.

Aggregate of complex shape can be further generated by rotating, scaling and moving the local meshes:

$$P_i''(x,y,z) = \mathbf{C}_{rot}\mathbf{D}_{move}\mathbf{E}_{scale}P_i'(x,y,z) \tag{2}$$

C, D and E represent the local rotating, moving and scaling matrix, respectively. Catmull–Clark subdivision surface algorithm [36] is used to smooth the mesh of aggregates by iterations. The point of face and edge can be expressed by:

$$v_F = \sum_{i=1}^{n} \frac{1}{n} v_i \,, v_E = \frac{v + u + v_{F_1} + v_{F_2}}{4} \tag{3}$$

Where, V_F, V_E, are the number of points of a face F and edge E. *v* and *u* represent the endpoint of the edge E and F_1, F_2 are the adjacent faces of the edge E. The new points are generated by:

$$v' = \frac{1}{n} Q + \frac{2}{n} R + \frac{n-3}{n} v \tag{4}$$

Where, Q, R are the average of adjacent face points with point v and R is the average of the midpoint of adjacent face points with point v. Aggregates with smooth surface can also be obtained through Catmull–Clark subdivision. If the subdivision surface were in-plane, it is entitled as a simple Catmull–Clark subdivision.

2.1.3 Displacement mapping and Laplace smoothing

A local weight displace mapping is developed to obtain aggregates of rough surface texture. Displacement mapping algorithm is expressed by [36]:

$$\mathbf{P}'(u,v) = \mathbf{P}(u,v) + d(u,v) \cdot \mathbf{n}(u,v) \tag{5}$$

Where $\mathbf{P}(u,v)$, $\mathbf{P}'(u,v)$ are the initial surface and update surface sets. $d(u,v)$ is the displacement and $\boldsymbol{n}(u,v)$ is the normal field of the surface. However, the surface reflects a Gibbs phenomenon [38] if a complex texture is directly used. Based on the displacement mapping algorithm, a local weight displacement mapping can be rewritten as follow:

$$\mathbf{P}'(u,v)=\mathbf{P}(u,v)+\left[w(u,v)\right]\cdot d(u,v)\cdot\mathbf{n}(u,v) \tag{6}$$

Where, $\left[w(u,v)\right]$ is the local weight vector, and if the whole surface is weighted by a constant, $\left[w(u,v)\right]$ it is simple as w=C.

As shown in Fig. 4, a 2×2 mm plane (Fig. 4(a)) is generated to add rough surfaces with distorted noise texture (Fig. 4(b)). The surface of the plane shows sharp features if only displace mapping algorithm implemented (as shown in Fig. 4(c), here w means the displacement mapping factor). By combining displacement mapping algorithm, Catmull–Clark subdivision and Laplace smoothing algorithm, the realistic surface texture can be obtained. As indicated in Fig. 4(d)-(f), the plane surface tends to be smooth when the number of iterations- n_{itr} of Catmull–Clark subdivision is equal to 3. When the Laplace smoothing factor- λ increases from -0.1 to 0.1(avoiding a distorted mesh), the hump displacement also goes up (Fig. 4(d)- Fig. 4(e)).

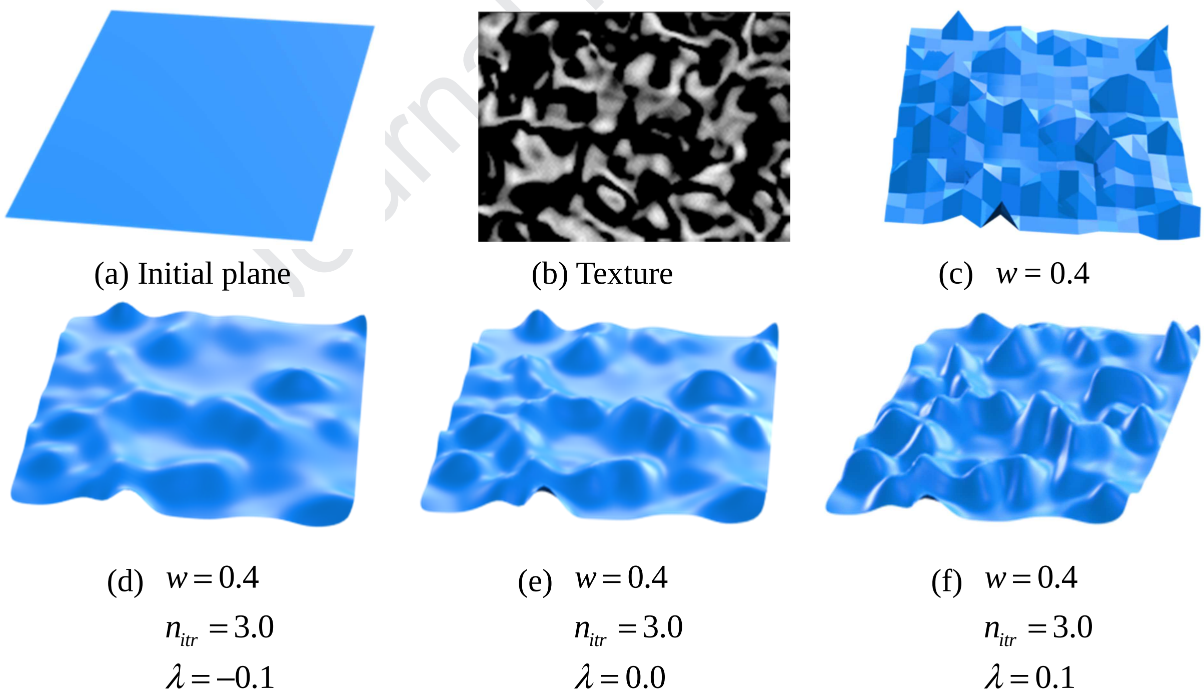

Fig. 4 Modeling of non-smooth plane surface

By adopting the abovementioned methods, realistic aggregates can be constructed. Figs. 5-6 show the generation process of crushed stone-like aggregate and gravel-like aggregate. It contains four steps as follows. At step 1, an initial icosahedron with the edge length of 1mm and a cloud texture were selected. The texture should be chosen based on the real situation. Displace mapping ($w=0.2$), Simple Catmull-Clark subdivision ($n_{sitr}=3.0$) and Laplace smoothing ($\lambda=0.2$) were implemented, respectively. However, the surface roughness of aggregate is still not clear as indicated in Fig. 5. Distorted noise texture was used at step 3 to further modified the aggregate surface so as to make it closer to the realistic, and Displace mapping (w=0.05), Simple Catmull-Clark subdivision ($n_{sitr}=3.0$) and Laplace smoothing ($\lambda=0.0$) were implemented to improve the accuracy of generated aggregates. A step 4, the coordinate of the initial icosahedron was randomly transformed. It should be noted that simple Catmull-Clark subdivision is used to generate crushed stone-like aggregate, while gravel-like aggregate should be constructed by Catmull-Clark subdivision. Gravel-like aggregates and crush stone-like aggregates generated by the proposed model are shown in Figs. 7-8.

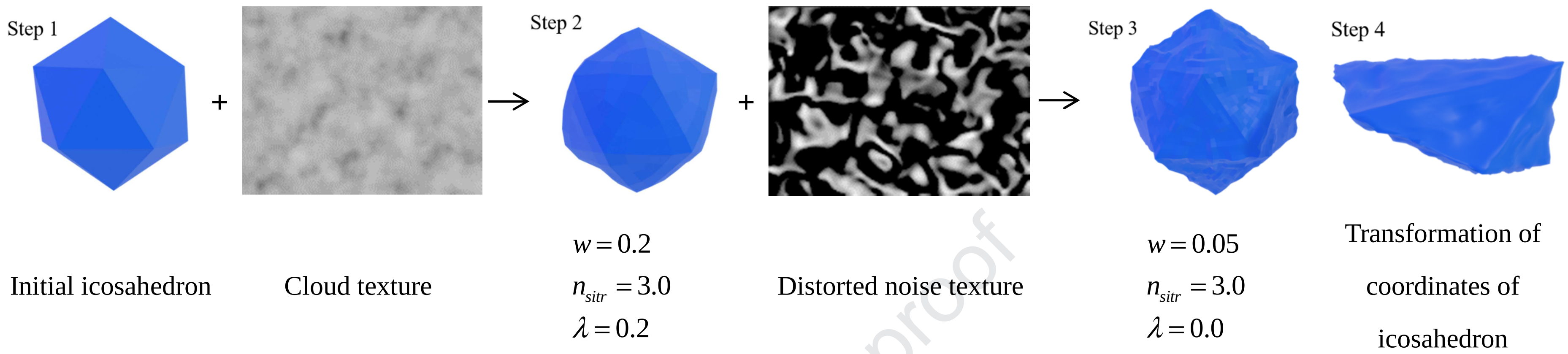

Fig. 5 Generation of crushed stone-like aggregate

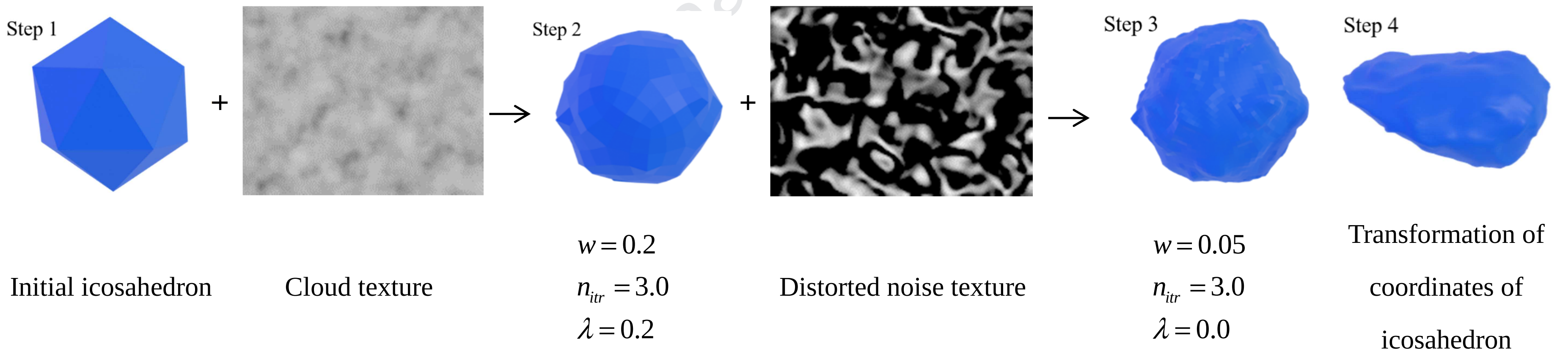

Fig. 6 Generation of gravel-like aggregate

In general, cell fracture algorithm can be used to generated aggregates of arbitrary shape. Catmull–Clark subdivision algorithm is used for obtaining the smooth surface of gravel-like aggregate, while crushed stone-like and gravel-like aggregates of rough surface texture can be generated by Texture displacement mapping, surface subdivision algorithm and Laplace smoothing algorithm.

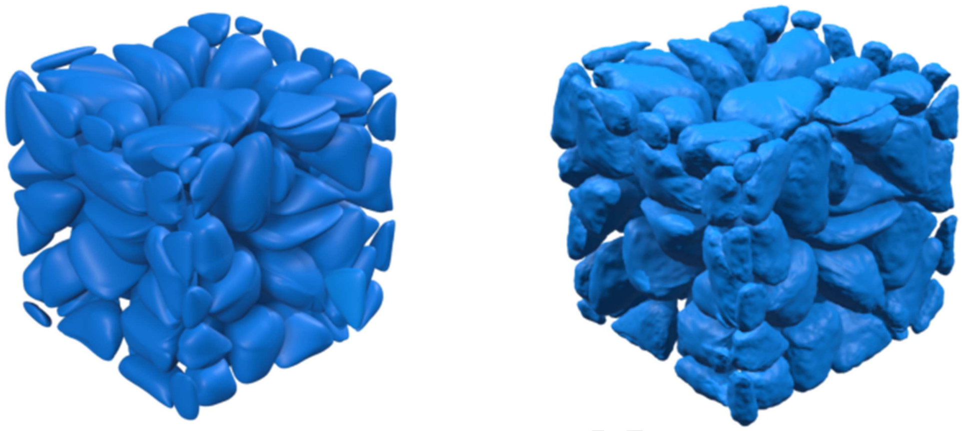

(a) Catmull–Clark subdivision algorithm

(b) Texture displacement mapping and Laplace smoothing algorithm

Fig. 7 Gravel-like aggregate with smooth and rough surface texture

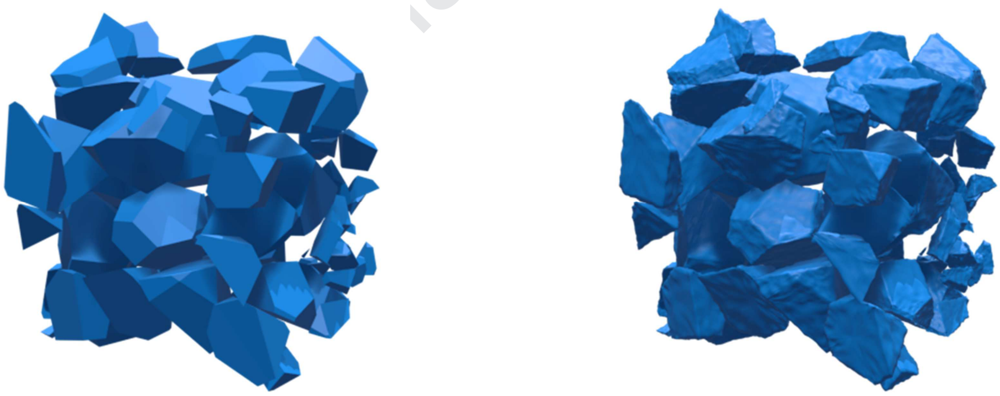

(e) Cell fracture algorithm and collision algorithm

(f) Surface subdivision algorithm and displacement mapping algorithm

Fig. 8 Crushed stone-like aggregate with smooth and rough surface texture

2. 2 Verified the gradation of aggregates generated by the proposed method

It's well known that the gradation of aggregates has a significant influence on the workability, mechanical performance and durability of concrete. To verify the simulation results obtained by the proposed method, Fuller distribution function according to our previous study [39] was used to represent the gradation curve of aggregate.

$$Y = 100(D / D_{\max})^{k} \tag{7}$$

Where, Y is the volume fraction of aggregate, D and D_{max} are the aperture diameter and the maximum diameter of aggregate, respectively, and k is the factor index.

For non-spherical aggregate, the equation can be rewritten as [40]:

$$Y = 100(D_{eq} / D_{\max eq})^{k} \tag{8}$$

Where, D_{eq} and D_{maxeq} represent the aperture diameter and the maximum diameter of non-spherical aggregate, respectively.

2. 3 Generation of fibers

Fibers can be easily constructed by Euclidean geometry at mesoscale. The size and shape of fibers in this study are referred to the previous work [41], as described in Fig. 9. For linear fiber, only two parameters (*i.e.*, length l =13 mm and radius r= 0.1 mm of cross-section) are required. As for hooked fiber, three different lengths l_1=1 mm, l_2=3 mm, l_3 =6 mm, the radius r_1= 0.25 mm at hooked region and the radius r= 0.1 mm of cross-section need to be determined.

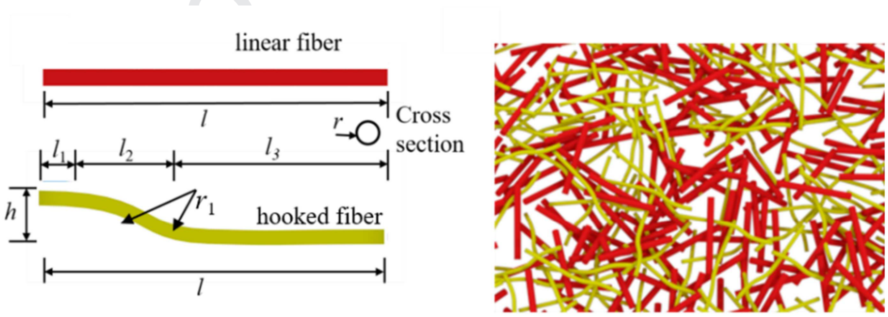

(a) Parameters of fibers (b) Mixture of fibers

Fig. 9 The parameters and mixture of fibers

2. 4 Dynamic mixing of aggregates and fibers

Collision algorithm is a good method for mixing the fibers and aggregates although they are generated by different methods. The framework of mixing procedure is shown in Fig. 10.

The particle emitter is first used to randomly generate all random points in the concrete model.

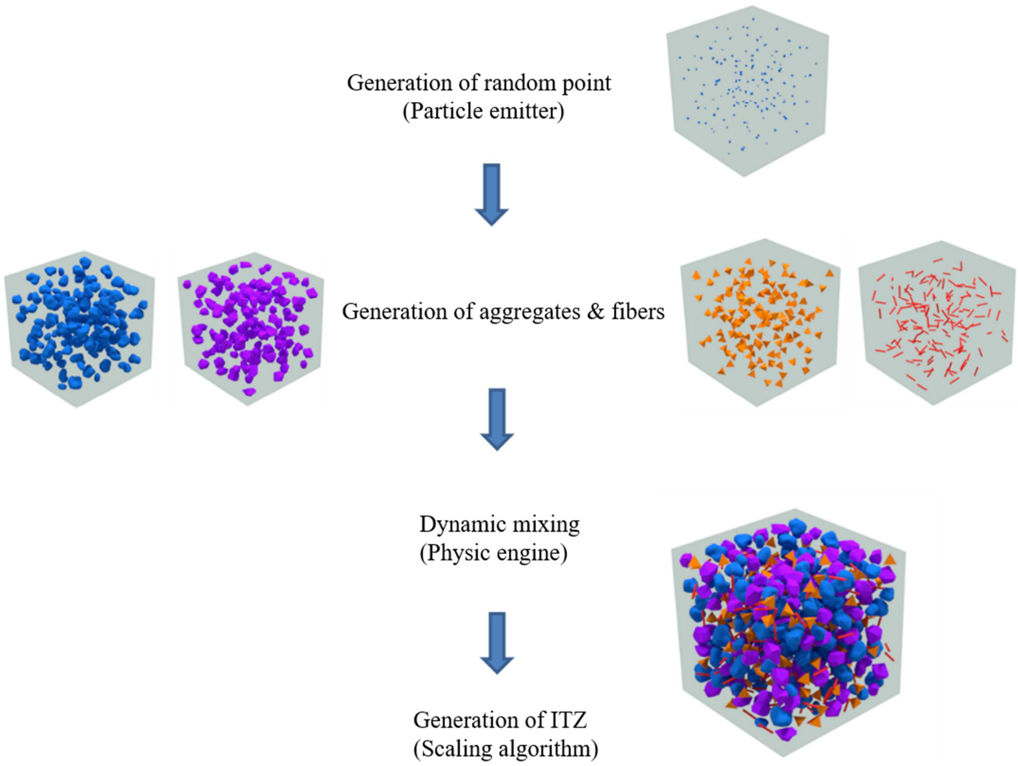

Fig. 10 Schematic diagram of dynamic mixing process of aggregates and fibers

Then, aggregates with surface texture were generated by the proposed method, and fibers were constructed by Euclidean geometry method. At last, the dynamic mixing process of fibers and aggregates is simulated by the rigid body collision algorithm in physical engine. In this step, fibers and aggregates are defined as rigid bodies. In order to ensure the uniform distribution of aggregates and fibers in concrete, the gravity acceleration of bodies is randomly defined as a negative or positive value.

$$X_{part} = X_{avg} + randn \cdot V \tag{9}$$

Where, X_{part} and X_{avg} are the coordinates of each part and average of unit model, respectively. V is the volume of unit model and the range of *randn* is [-1/2,1/2].

As shown in Figs. 11 and 12, the motion equation of rigid bodies can be written as below:

$$\frac{d}{dt}\mathbf{X}(t)=\frac{d}{dt}\begin{bmatrix}\mathbf{X}(t)\\ \mathbf{R}(t)\\ \mathbf{P}(t)\\ \mathbf{L}(t)\end{bmatrix}=\begin{bmatrix}\mathbf{v}(t)\\ \boldsymbol{\omega}(t)\cdot\mathbf{R}(t)\\ \mathbf{F}(t)\\ \boldsymbol{\tau}(t)\end{bmatrix} \tag{10}$$

Where, $\mathbf{X}(t)$ is position vector, $\mathbf{R}(t)$ is orientation vector, $\mathbf{P}(t),\mathbf{L}(t)$ are the linear momentum vector and angular momentum vector, respectively. $\mathbf{v}(t),\boldsymbol{\omega}(t)$ represent the velocity vector and angular velocity vector, respectively. $\mathbf{F}(t),\boldsymbol{\tau}(t)$ represent force vector and torque vector, respectively.

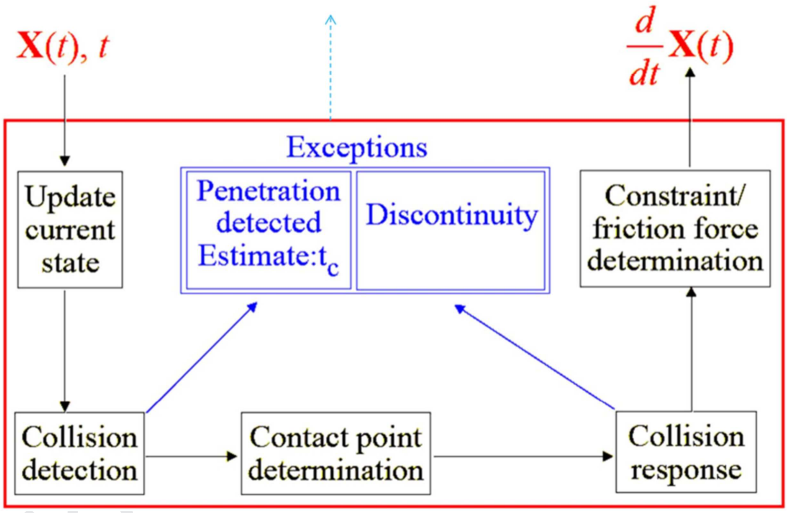

Fig. 11 Illustration of collision detection [42]

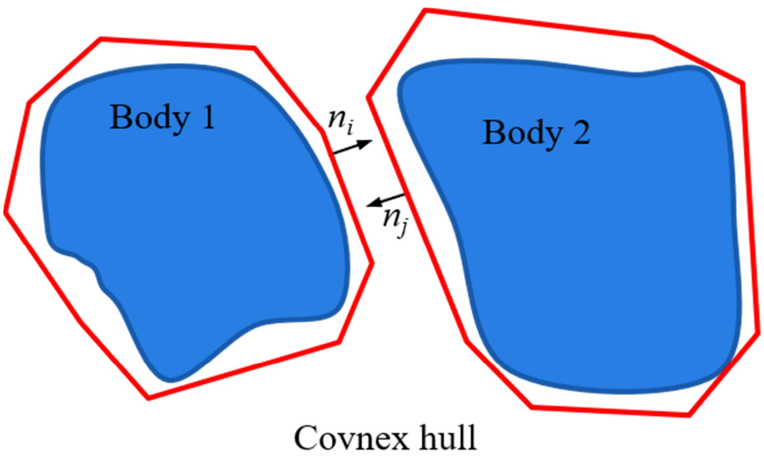

Fig. 12 Collision detection between two rigid bodies

Fig. 11 shows the mixing process of realistic aggregates and fibers. Realistic aggregates and fibers are firstly generated and randomly distributed in the model, then the overlapping of aggregates and fibers are detected. If the overlaps are detected, the positions of aggregates and fibers are updated until there does not exist any coincidence in the model. To reduce the calculation time, the collision detection algorithm was applied in the axis aligned bounding box (AABB). This means that all bodies are constrained with bound convex-hull, as shown in Fig. 12. The minimum distance D_{dis} is determined by calculating the distance of the nearest adjacent points in the boundary of rigid body. When D_{dis} is negative, the intersections of adjacent rigid bodies are detected, and the positions of rigid bodies are updated. The whole process takes a very short time. This process terminates once there does not exist intersections of all rigid bodies in the system.

2. 5 Generation of the ITZ

The ITZ is generally simplified as an annular region with a certain thickness around the aggregates and fibers [6, 43, 44], as shown in Fig. 13 [32]. The ITZ is a weak but important region in concrete, which significantly affects its compressive strength [43], tensile strength [44] and failure behavior. The thickness and morphology of ITZ [45] are determined by raw materials, mix proportion, curing condition, etc.

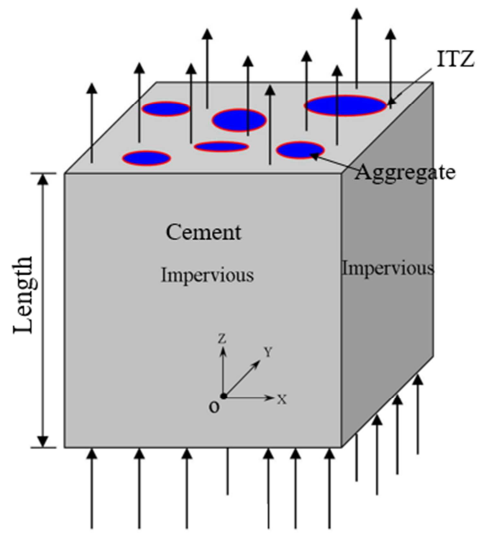

Fig. 13 Mesoscale concrete model with cement pastes, aggregates and ITZs [32].

Scaling algorithm was adopted in this work to obtain the ITZ of fibers and aggregates, as shown in Fig. 14. The centroid centers coordinates are determined by the equation as follows:

$$\overline{x}=\frac{\int_V xdV}{\int_V dV},\overline{y}=\frac{\int_V ydV}{\int_V dV},\overline{z}=\frac{\int_V zdV}{\int_V dV} \tag{11}$$

Where, x, y, z are the coordinate of centroid centers C_r, respectively. Particle with arbitrary shape can be approximately divided by 3D Delaunay triangulation algorithm, so that the equation can be further simplified as follow:

$$\overline{x}=\frac{\sum x_i V_i}{\sum V_i},\overline{y}=\frac{\sum y_i V_i}{\sum V_i},\overline{z}=\frac{\sum z_i V_i}{\sum V_i} \tag{12}$$

Where x_i, y_i, and z_i represent the centroidal coordinates of Delaunay triangulations, respectively.

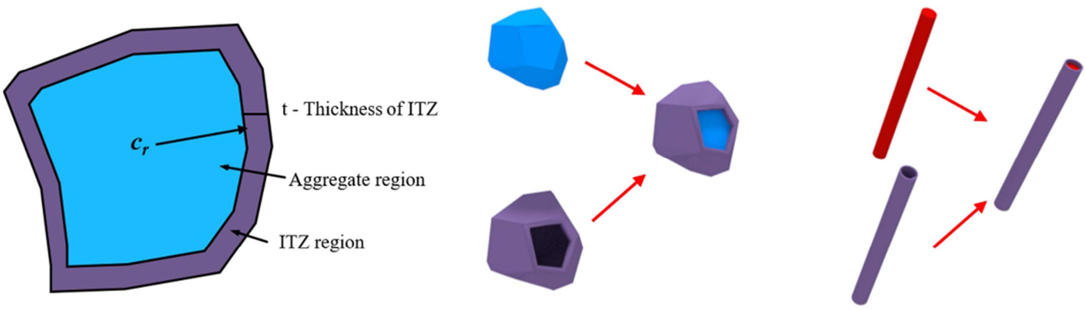

(a) Illustration of aggregate with the ITZ (b) Aggregate and the ITZ (c) Fiber and the ITZ

Fig. 14 Illustration of aggregate and fiber containing the ITZ

3. Mesoscale models of plain and fiber reinforced concretes

The structures of plain and fiber reinforced concretes generated by the proposed method are shown in Figs. 15-18. In order to show it more intuitively, the dynamic processes of the cross-section diagrams of plain and fiber reinforced concretes mesoscale models are attached in the data files, and the details are described in the following sections.

3. 1 Mesoscale model of two-graded aggregate concrete

As illustrated in Fig. 15, the minimum effective diameter of realistic aggregate is 4.75 mm and the maximum one is 38 mm, which is in accordance with experimental data [46]. Each aggregate is generated by the proposed method and there do not exist the exactly same aggregates in the model. The overlaps of aggregates are detected and each aggregate are uniformly distributed. To validate that the generated model meets the requirements of aggregate gradation, the simulation results are compared and shows a good agreement with the experimental data, as indicated in Fig. 16.

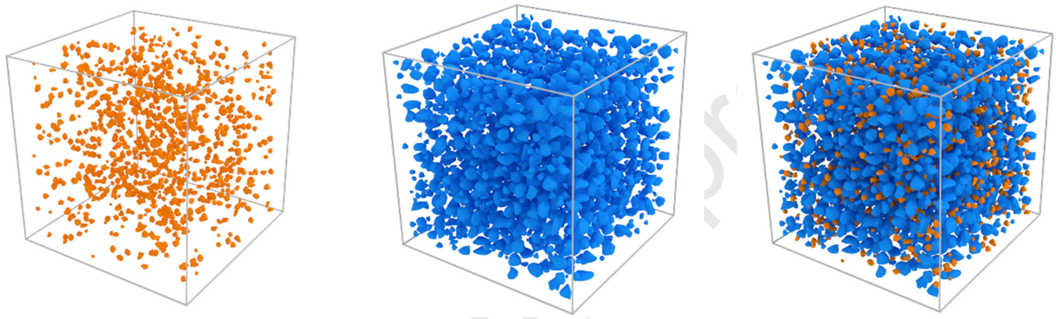

(a) Aggregates (4.75-19 mm) (b) Aggregates (19-38 mm) (c) Two-graded mesoscale concrete model

Fig. 15 Generation of two-graded mesoscale concrete models

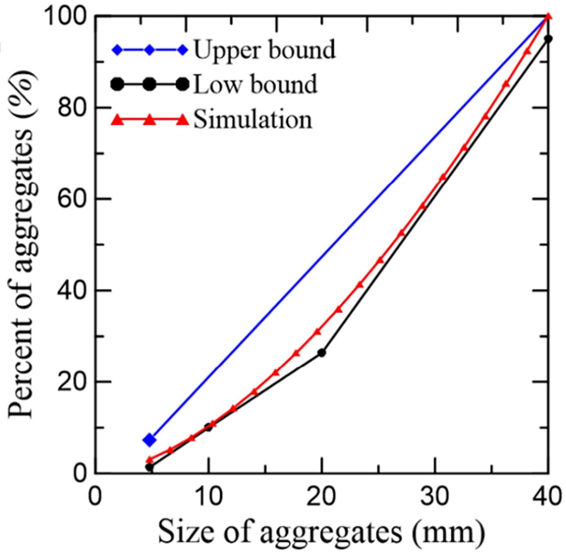

Fig. 16 Gradation curves of aggregates in this work (Upper and low bound curves are from [46])

3. 2 Mesoscale model of hybrid fiber reinforced concrete

To construct mesoscale model of hybrid fiber reinforced concrete, four steps should be adopted: (1) Construct realistic aggregates by the proposed approach, this steps can be divided into five parts as follows: (1a) Generate an arbitrary-shaped aggregate based on Euclidean geometry algorithm; (1b) Obtain realistic aggregates by cell fracture algorithm; (1c) Realistic surface texture of aggregate is generated by the iterations of surface subdivision (Catmull–Clark subdivision algorithm), displacement mapping and Laplace smoothing; (1d) Validation of the aggregate gradation; (1e) Define all aggregates as active bodies. Active body only defines the initial position, it can move freely to collide with other particles. While passive body limit the boundary and movement of particles, so the location can not be changed when calculated by collision algorithm. (2) Euclidean geometric formula was adopted to generate long hooked and short straight fibers. In contrast to the generation process of realistic aggregate, all the fibers are defined as active bodies at this step. (3) Mix all the aggregates and fibers according to the collision algorithm and detect the overlaps of fibers and aggregates; (4) Construct the ITZ by the scaling algorithm, as illustrated in Fig. 17.

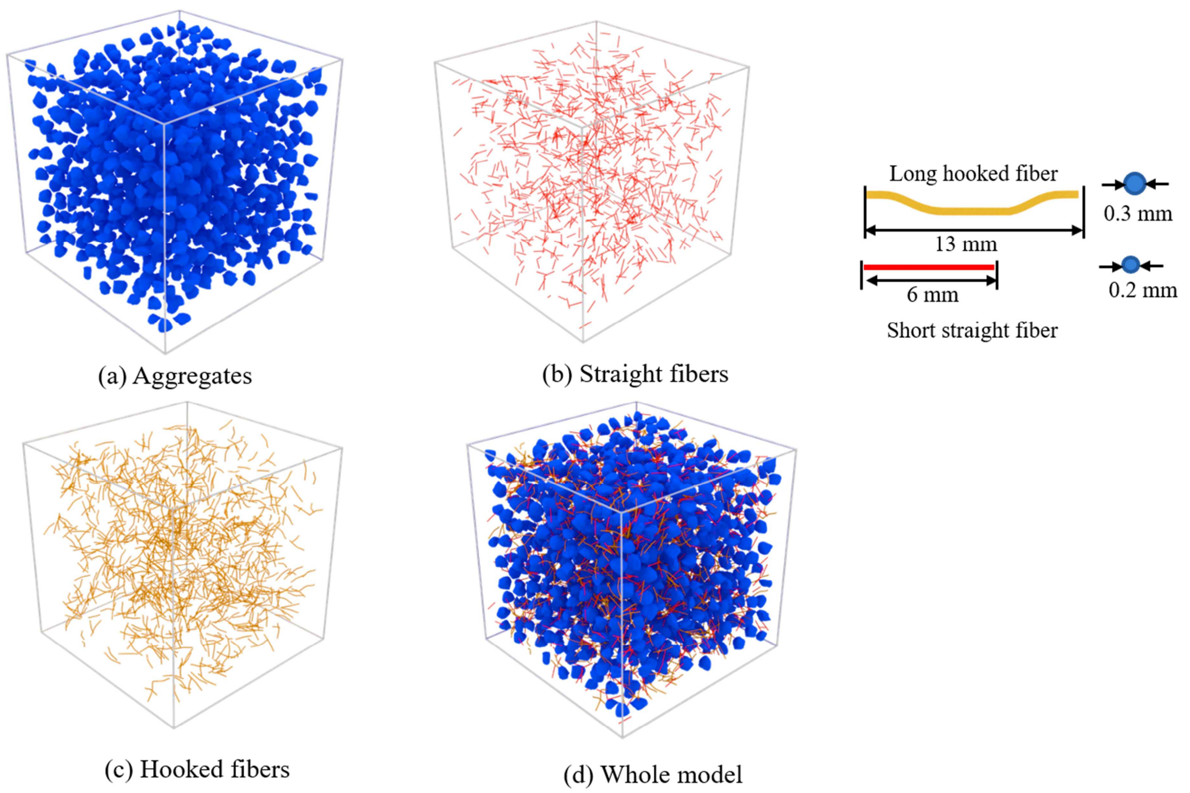

Fig. 17 Mesoscale model of hybrid fiber reinforced concrete

3. 3 Mesoscale model of aligned fiber reinforced concrete

In order to obtain the mesoscale model of aligned fiber reinforced concrete, fibers were firstly generated and located at random location in unit concrete model. Then, all the fibers should be defined as passive bodies so that the location and direction of fibers is unchanged. Next, aggregates generated by the proposed method are defined as active bodies with gravity at Z-direction and were poured into concrete model. At last, aggregates in concrete were redistributed according to the collision algorithm until there does not exist any overlaps. This process is shown in Fig. 18.

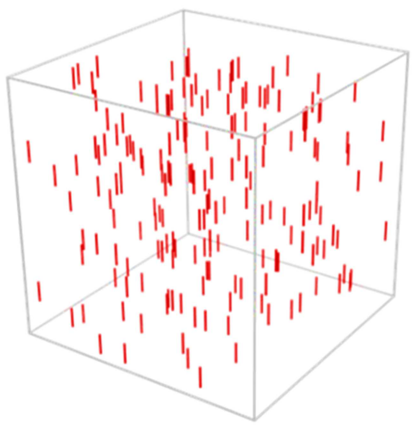

(a) Aligned short straight fibers

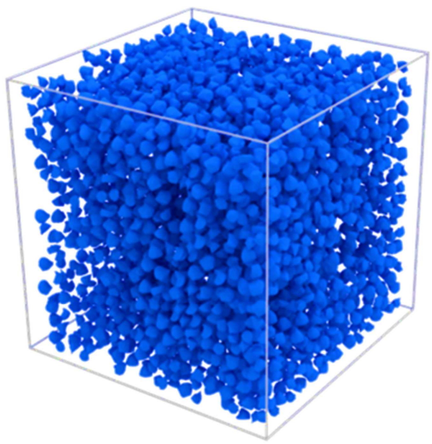

(b) Aggregates

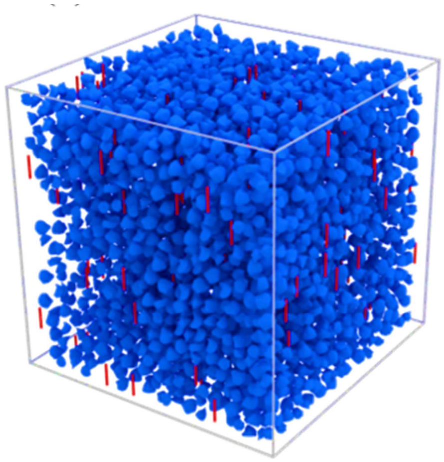

(c) FRC with aligned fibers

Fig. 18 Generation of FRC mesoscale model with aligned fibers

4. Properties analysis on 3D mesoscale models for plain and fiber reinforced concretes

4. 1 The volume fraction of the ITZ

Mesoscale model is the common, convenient and economical method to study the volume fraction of the ITZ in concrete. It is reported that the volume fraction of the ITZ goes up at the increased aggregate content based on 2D and 3D concrete mesoscale models [40, 47]. However, previous studies always use 2D and 3D regular aggregates, the real situation cannot be fully reflected. On the basis of the proposed plain and fiber reinforced concrete mesoscale model, the influence of realistic aggregate and fiber on the volume fraction of the ITZ are presented as follows.

4.1.1 Effect of aggregate size on the volume fraction of the ITZ

According to the previous work [48], the ITZ thicknesses are found to be 25 μm, 35-34 μm, 45 μm and 50 μm for limestone aggregate of various sizes (*i.e.* 5 mm, 10 mm, 20 mm and 30 mm), respectively. The thickness of ITZ tends to be stable when the aggregate size is larger than 30 mm. As illustrated in Fig. 19(a), the relationship between the ITZ thickness and the size of aggregate can be expressed as a function: $f(t) = 17.52\sqrt{D_{\max eq}}\text{-}1.274D_{\max eq} - 7.757$, D_{maxeq} represents the maximum diameter of aggregates. Fig. 19(b) shows that the volume fraction of the ITZ goes up with the increase of the volume fraction of aggregate when D_{mineq} (the minimum diameter of aggregates) is equal to 5 mm. However, the volume fraction of ITZ decreases with the increase of the maximum equivalent particle size of aggregates. The reason is that the total surface area of aggregate decreases as the D_{maxeq} increases, resulting in a decline in the volume fraction of the ITZ.

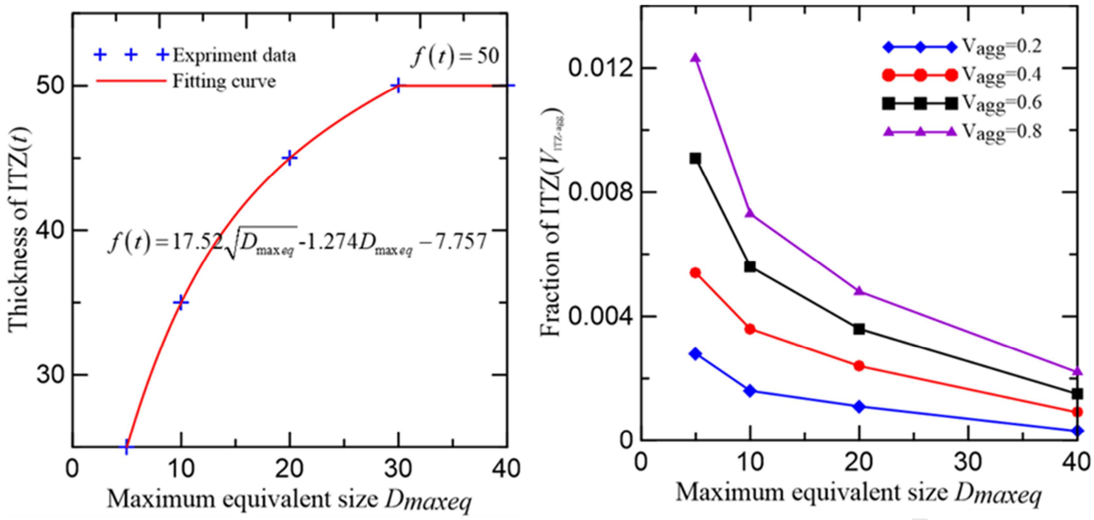

(a) Relationship between t and D_{maxeq} (b) Relationship between V_{ITZ} and D_{maxeq} with various V_{agg}

Fig. 19 t and $V_{ITZ-agg}$ versus the maximum size D_{maxeq} of aggregate

4.1.2 Effect of aggregate gradation on the volume fraction of the ITZ

Fig. 20 shows the influence of aggregate gradation on the volume fraction of ITZ. The thickness of the ITZ and the gradation of aggregates are in accordance with the experiment [48]. It is found that as the gradation of aggregates increases, the volume fraction of the ITZ goes down. The volume fraction of the ITZ falls in the order: one-gradation level>two-gradation level. In other words, the larger aggregate gradation of concrete, the smaller volume fraction of ITZ when the ITZ thickness is a constant.

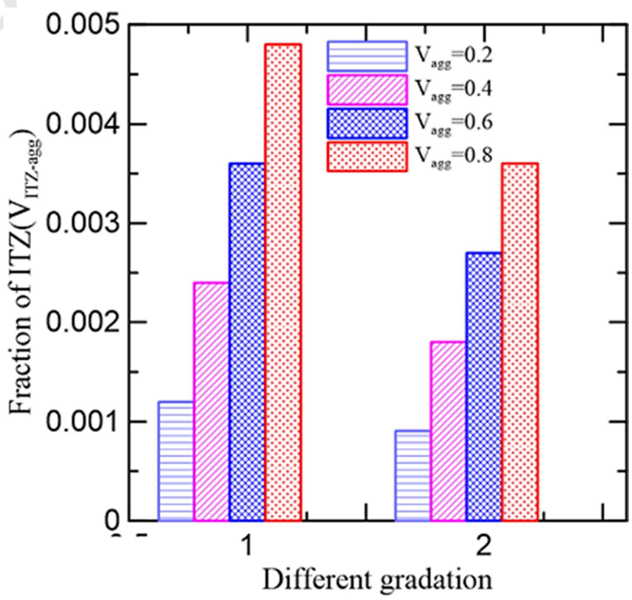

Fig. 20 Volume fraction of ITZs-V_{ITZ} at different aggregate gradation

4.1.3 Effect of fiber amount on the volume fraction of the ITZ

According to the previous work [49], the ITZ thickness between fiber and cement paste is equal to 0.04 mm when the curing age is 28 days for UHPC with water-binder ratio of 0.18 and 20% silica fume. As shown in Fig. 21, the volume fraction of the ITZ (V_{ITZ}) almost linearly goes up with the increase of the volume fraction of fiber (V_f). The reason is that fibers are uniformly dispersed in concrete mesoscale model, and the size and volume fraction of fiber are not high, so there does not exist overlapping of the ITZ between fibers and paste. Hence, the volume fraction of the ITZ can be expressed as below:

$$V_{ITZ} = \frac{((R+t)^2 - R^2)}{R^2}\frac{(l-2t)}{l}V_f \tag{13}$$

Where, *R*, *l* are the radius and length of fiber, respectively. t is the thickness of the ITZ, and V_f represents the volume fraction of fibers. It can be seen that *l*>>t, so the Eq. (16) can be further simplified:

$$V_{ITZ} = \frac{((R+t)^2 - R^2)}{R^2}V_f \tag{14}$$

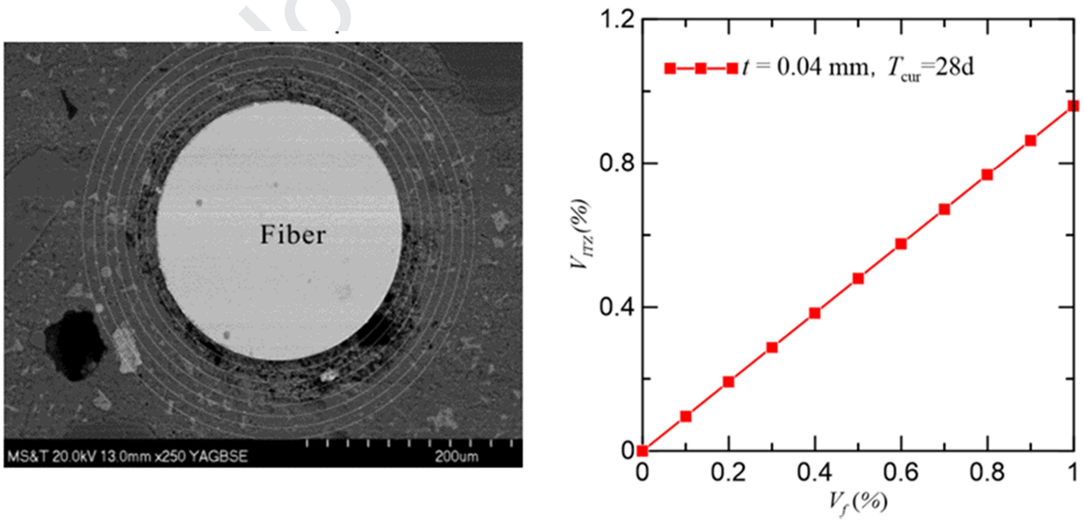

(a) BSEM images of ITZ of UHPC with 20% silica fume and fiber at 28d [49]

(b) V_{ITZ} versus V_f

Fig. 21 Effect of fiber on the thickness and volume fraction of the ITZ

4.2 Prediction of the elastic modulus of plain and fiber reinforced concretes

On the basis of the obtained volume fraction of the ITZ, the effective elastic modulus of concrete can be predicted. Although three-phase micromechanical model for hybrid fiber reinforced concrete [50] has been used before, this model only takes spherical aggregates or regular aggregates into account. Combing Monte Carlo simulation and the proposed mesoscale model, the effective elastic modulus of plain and fiber reinforced concretes can be determined.

On the basis of the Hashin's solution [51], Qiu *et al*. [52] proposed an exact solution to compute the effective elastic modulus of three-phase concrete, for four-phases fiber reinforced concrete, the equation can be expressed as follows in this work:

$$K_{eff} = K_{con} + \frac{\left(K_{con} + 4/3G_{con}\right)\left[A_{12} + B_{12}\left(K_{agg/fiber} + 4/3G_{ITZ}\right)\right]}{-A_{12} - 4/3\frac{V_{agg/fiber}}{\left(V_{agg/fiber} + V_{ITZ}\right)}\left(G_{con} - G_{ITZ}\right) + \left(K_{agg/fiber} + 4/3G_{ITZ}\right)\left(\frac{K_{ITZ} + 4/3G_{con}}{K_{agg/fiber} - K_{ITZ}} - B_{12}\right)} \tag{15}$$

Where,

$$A_{12} = V_{agg/fiber}\left(K_{con} + 4/3G_{ITZ}\right), \quad B_{12} = \left(V_{agg/fiber} + V_{ITZ}\right)\frac{K_{ITZ} - K_{con}}{K_{agg/fiber} - K_{ITZ}} \tag{16}$$

Where, K_{con}, $K_{agg/fiber}$, K_{ITZ} are the bulk modulus of concrete, aggregates or fiber, and ITZ, respectively. G_{con}, $G_{agg/fiber}$ and G_{ITZ} represents the shear modulus of concrete, aggregates or fiber, and ITZ, respectively. $V_{agg/fiber}$ represents volume fraction of aggregate or fiber. There exists a relationship between the abovementioned parameters and Poisson's ratio as below:

$$K_i = \frac{E_i}{3\left(1 - 2v_i\right)}, \quad G_i = \frac{E_i}{2\left(1 + v_i\right)} \tag{17}$$

Where, *i* represent the symbol of cement, aggregates and ITZ. According to the previous research [53], E_{con}=75.5GPa, E_{agg}=11.6 GPa, E_{ITZ}=45.3 GPa. v_{con}=0.35, v_{agg}=0.15 and v_{ITZ}=0.35, and the thickness of ITZ is 40 μm [49]. The effective modulus can be calculated as follows:

$$E_{eff} = 3K_{eff}(1-2v_{eff}) \tag{18}$$

The ITZ thickness and the properties of cement matrix are kept the same in this study according to the experimental data [48]. The effective elastic modulus of concrete (E_{eff}) containing aggregates of various shapes is calculated by the Monte Carlo method. It can be seen from Fig. 21 that the predicted results of E_{eff}/E_{bk} (E_{bk} is the bulking modulus of concrete) agree well with the experimental data [53]. It shows that the aggregate shape does not significantly affect the effective elastic modulus of concrete when the effective maximum diameter D_{eqmax} of aggregates is less than 20 mm.

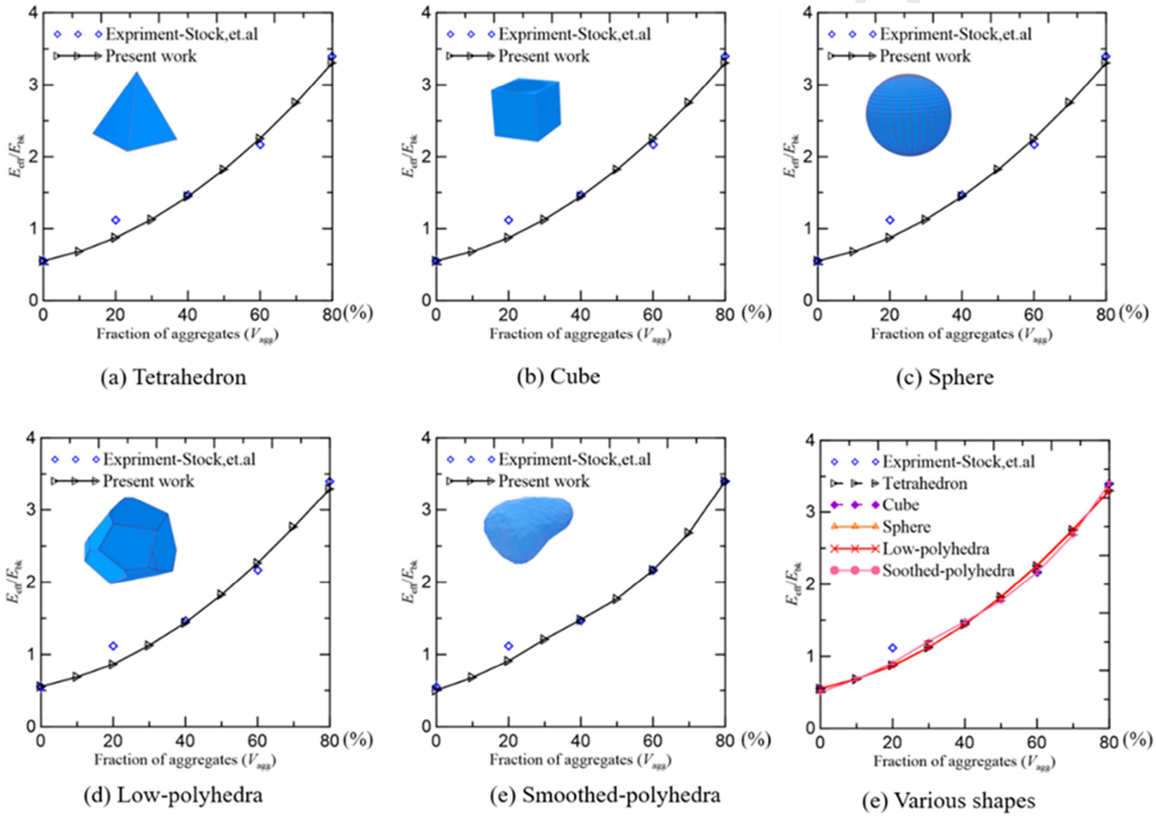

Fig. 22 Comparisons of simulation results and experimental data for the effective elastic modulus of concrete (aggregate size ranges from 2.4 mm to 19 mm)

Furthermore, the developed models can be applied to calculate the Young's modulus of hybrid fibers reinforced concrete. The models are shown in section 3. 2 in this paper. According to the literature [54], the Young's modulus of cement E_c=33.6 GPa, the passion ratio v_c=0.15. For steel fibers, the Young's modulus E_s and Possion ratio v_s are 210 GPa and 0.3, respectively. The volume fraction of long fibers and short fibers are both 1%.

Experimental data [54] and simulation results both indicate that the Young's modulus of UHPC containing hybrid fibers reaches the maximum value when the volume fraction of long and short fibers are 1.5% and 0.5%, as demonstrated in Fig. 23. It can also be found that the numerical results are slightly smaller than the experimental data. This may be attributed to the fact that the thickness of ITZ is assumed to be a constant in this work, resulting in a lower effective Young’s modulus of UHPC. In real situations, ITZ is not constant and needs further study.

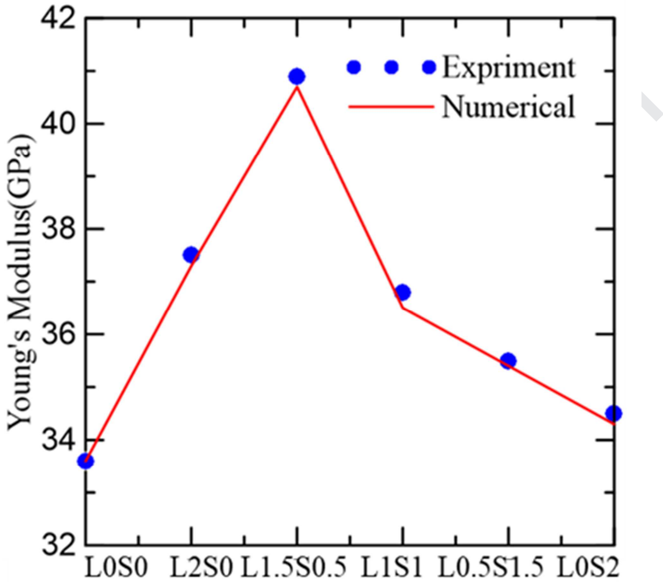

Fig. 23 Effective elastic modulus of UHPC with hybrid fibers

(“L” represents “long steel fiber”, “S” represents “short steel fiber”, “L0S0” is referred to UHPC with no fiber, and L1.5S0.5 represents UHPC with 1.5% long steel fiber and 0.5% short steel fiber.)

5. Conclusions

This work presents a promising, reliable and useful tool to generate plain and fiber reinforced concretes 3D mesoscale model. Realistic aggregates with rough surface texture can be well represented by the proposed method. The influence of aggregates and fibers on the ITZ volume fraction and mechanical properties of concrete are thus quantitatively studied. Main conclusions can be drawn as follows:

(1) By combing modified cell fracture, Catmull–Clark subdivision, texture displacement and Laplace smoothing algorithm, realistic aggregates with rough/smooth surface texture can

be generated.

(2) Physics engine is applied to construct plain and fiber reinforced concretes mesoscale models. The shape, aggregate gradation, random and aligned fibers can be taken into account. Collision algorithm is an effective approach to model the dynamic mixing process of fibers and aggregates in concrete.

(3) The volume fraction of the ITZ is found to go down with the increase of the gradation and D_{maxeq} of aggregate, and go up at the increased fiber volume fraction when fibers are uniformly distributed in concrete.

(4) The effective elastic modulus of plain and fiber reinforced concretes can be well predicted. A good agreement with the experimental data is observed, validating the proposed model.

(5) Generating a reliable model is helpful for providing in-depth insights and can be widely applied to study the properties of plain and fiber reinforced concretes combined with finite element method, discrete element method, etc. in further works.

Acknowledgment

The authors gratefully acknowledge the financial support from the Chinese Ministry of Science and Technology under Project (Grant No. 2018YFC0705400), and National Science Foundation of China under Project (Grant No. 201601370519), and financial support from the program of China Scholarships Council (CSC No. 201906130089), as well as the Hunan Provincial Innovation Foundation for Postgraduate (CX2018B220).

Reference

[1] C. Shi, Z. Wu, J. Xiao, D. Wang, Z. Huang. Z. Fang. A review on ultra high performance concrete: Part I. Raw materials and mixture design, Constr Build Mater., 101 (2015) 741-751. https://doi.org/10.1016/j.conbuildmat.2015.10.088

[2] J.D. Ríos, H. Cifuentes, C. Leiva, S. Seitl, Analysis of the mechanical and fracture behavior of heated ultra-high-performance fiber-reinforced concrete by X-ray computed tomography, Cem Concr Res, 119 (2019) 77-88. https://doi.org/10.1016/j.cemconres.2019.02.015

[3] A. Qsymah, R. Sharma, Z. Yang, L. Margetts, P. Mummery, Micro X-ray computed tomography image-based two-scale homogenisation of ultra high performance fibre reinforced concrete, Constr Build Mater., 130 (2017) 230-240. https://doi.org/10.1016/j.conbuildmat.2016.09.020

[4] O. Yılmaz, J.F. Molinari, A mesoscale fracture model for concrete, Cem Concr Res, 97 (2017) 84-94. https://doi.org/10.1016/j.cemconres.2017.03.014

[5] P. Wriggers, S. Moftah, Mesoscale models for concrete: Homogenisation and damage behaviour, Finite Elem Anal Des, 42 (2006) 623-636. https://doi.org/10.1016/j.finel.2005.11.008

[6] R. Zhou, Z. Song, Y. Lu, 3D mesoscale finite element modelling of concrete, Comput Struct, 192 (2017) 96-113. https://doi.org/10.1016/j.compstruc.2017.07.009

[7] P. Sheng, Z. Chen, J. Zhang, Z. Ji, Evolution and heredity of particle distribution in the free-fall method of modeling particle-reinforced concrete-like composites, Powder Technol., 353 (2019) 1-9. https://doi.org/10.1016/j.powtec.2019.04.083

[8] Z. Qian, E. Garboczi, G. Ye, E. Schlangen, Anm: a geometrical model for the composite structure of mortar and concrete using real-shape particles, Mater Struct, 49 (2016) 149-158. https://doi.org/10.1617/s11527-014-0482-5

[9] P. Stroeven, L.J. Sluys, Z. Guo, M. Stroeven, Virtual Reality Studies of Concrete, Forma, 21 (2006) 227-242.

[10] O. Yılmaz, J.-F. Molinari, A mesoscale fracture model for concrete, Cem Concr Res, 97 (2017) 84-94. https://doi.org/10.1016/j.cemconres.2017.03.014

[11] W. Xu, F. Wu, Y. Jiao, M. Liu, A general micromechanical framework of effective moduli for the design of nonspherical nano-and micro-particle reinforced composites with interface properties, Mater. Des., 127 (2017) 162-172. https://doi.org/10.1016/j.matdes.2017.04.075

[12] Q. Ren, G. De Schutter, Z. Jiang, Q. Chen, Multi-level diffusion model for manufactured sand mortar considering particle shape and limestone powder effects, Constr Build Mater., 207 (2019) 218-227. https://doi.org/10.1016/j.conbuildmat.2019.02.139Get rights and content

[13] Z. Xu, H. Hao, H. Li, Mesoscale modelling of dynamic tensile behaviour of fibre reinforced concrete with spiral fibres, Cem Concr Res, 42 (2012) 1475-1493.

https://doi.org/10.1016/j.cemconres.2012.07.006

[14] F. Nilenius, F. Larsson, K. Lundgren, K. Runesson, A 3d/2d comparison between heterogeneous mesoscale models of concrete, in: Multi-Scale Modeling and Characterization of Infrastructure Materials, Springer, 2013, pp. 249-259.

[15] H. Ma, W. Xu, Y. Li, Random aggregate model for mesoscopic structures and mechanical analysis of fully-graded concrete, Comput Struct, 177 (2016) 103-113. https://doi.org/10.1016/j.compstruc.2016.09.005

[16] L. Liu, D. Shen, H. Chen, W. Xu, Aggregate shape effect on the diffusivity of mortar, Comput Struct, 144 (2014) 40-51. https://doi.org/10.1016/j.compstruc.2014.07.022

[17] P.L. George, H. Borouchaki, Delaunay Triangulation and Meshing, Hermès, 1998.

[18] Z.M. Wang, A.K.H. Kwan, H.C. Chan, Mesoscopic study of concrete I: generation of random aggregate structure and finite element mesh, Comput Struct, 70 (1999) 533-544. https://doi.org/10.1016/S0045-7949(98)00177-1Get rights and content

[19] L. Song, B. Song, T. Shen, B. Yu, A New Numerical Simulation Method for Three-Dimensional Mesoscale Analysis of Concretes, Math. Probl. Eng., 2015, (2015-1-19), 2015 (2015) 1-7. http://dx.doi.org/10.1155/2015/627948

[20] G. Ma, W. Zhou, X.L. Chang, W. Yuan, Combined FEM/DEM Modeling of Triaxial Compression Tests for Rockfills with Polyhedral Particles, INT J GEOMECH, 14 (2014) 04014014. https://doi.org/10.1061/(ASCE)GM.1943-5622.0000372

[21] K. Dong, C. Wang, A. Yu, A novel method based on orientation discretization for discrete element modeling of non-spherical particles, Chem. Eng. Sci., 126 (2015) 500-516. https://doi.org/10.1016/j.ces.2014.12.059

[22] W. Chen, T. Donohue, A. Katterfeld, K. Williams, Comparative discrete element modelling of a vibratory sieving process with spherical and rounded polyhedron particles, Granul Matter, 19 (2017) 81. https://doi.org/10.1007/s10035-017-0749-y

[23] S. Erdogan, P. Quiroga, D.W. Fowler, H. Saleh, R.A. Livingston, E.J. Garboczi, P.M. Ketcham, J.G. Hagedorn, S.G. Satterfield, Three-dimensional shape analysis of coarse aggregates: New techniques for and preliminary results on several different coarse aggregates and reference rocks, Cem Concr Res, 36 (2006) 1619-1627.

https://doi.org/10.1016/j.cemconres.2006.04.003
[24] Z. Qian, Multiscale modeling of fracture processes in cementitious materials, 2012.
[25] J. Huang, Q. Peng, X. Hu, Y. Du, A combined-alpha-shape-implicit-surface approach to generate 3D random concrete mesostructures via digital image processing, spectral representation, and point cloud, Constr Build Mater., 143 (2017) 330-365. https://doi.org/10.1016/j.conbuildmat.2017.03.104
[26] X. Guan, X. Liu, X. Jia, Y. Yuan, J. Cui, H.A. Mang, A stochastic multiscale model for predicting mechanical properties of fiber reinforced concrete, Int J Solids Struct, 56 (2015) 280-289. https://doi.org/10.1016/j.ijsolstr.2014.10.008
[27] X. Liang, C. Wu, Meso-scale modelling of steel fibre reinforced concrete with high strength, Constr Build Mater., 165 (2018) 187-198. https://doi.org/10.1016/j.conbuildmat.2018.01.028
[28] Z. Xu, H. Hao, H.N. Li, Mesoscale modelling of fibre reinforced concrete material under compressive impact loading, Constr Build Mater., 26 (2012) 274-288. https://doi.org/10.1016/j.conbuildmat.2011.06.022
[29] E. Gal, R. Kryvoruk, Meso-scale analysis of FRC using a two-step homogenization approach, Comput Struct, 89 (2011) 921-929. https://doi.org/10.1016/j.compstruc.2011.02.006
[30] Z. Han, W. Xu, L. Tao, Q. Ding, H. Ma, Random non-convex particle model for the fraction of interfacial transition zones (ITZs) in fully-graded concrete, Powder Technol., 323 (2017) 301-309. https://doi.org/10.1016/j.powtec.2017.10.009
[31] H.L. Anderson, Metropolis, Monte Carlo and the MANIAC, Los Alamos Science, 14 (1986) 96-108.
[32] X. Li, Y. Xu, S. Chen, Computational homogenization of effective permeability in three-phase mesoscale concrete, Constr Build Mater., 121 (2016) 100-111. https://doi.org/10.1016/j.conbuildmat.2016.05.141
[33] W. Xu, H. Ma, S. Ji, H. Chen, Analytical effective elastic properties of particulate composites with soft interfaces around anisotropic particles, Compos Sci Technol, 129 (2016) 10-18. https://doi.org/10.1016/j.compscitech.2016.04.011

[34] J.R. Willis, Bounds and self-consistent estimates for the overall properties of anisotropic composites, J Mech Phys Solids, 25 (1977) 185-202. https://doi.org/10.1016/0022-5096(77)90022-9

[35] M. Zhang, Characteristics of lightweight aggregates for high strength concrete, ACI Mater J, 88 (1991) 150-158.

[36] E. Catmull, J. Clark, Recursively generated B-spline surfaces on arbitrary topological meshes, Comput Aided Des, 10 (1978) 350-355. https://doi.org/10.1016/0010-4485(78)90110-0

[37] H. Ledoux, Computing the 3D Voronoi Diagram Robustly: An Easy Explanation, in: International Symposium on Voronoi Diagrams in Science and Engineering, 2007, pp. 117-129. https://doi.org/10.1109/ISVD.2007.10

[38] A. Gelb, The resolution of the Gibbs phenomenon for spherical harmonics, Mathematics of Computation of the American Mathematical Society, 66 (1997) 699-717.

[39] W. Xu, Z. Lv, H. Chen, Effects of particle size distribution, shape and volume fraction of aggregates on the wall effect of concrete via random sequential packing of polydispersed ellipsoidal particles, Physica A Stat. Mech. Appl., 392 (2013) 416-426. https://doi.org/10.1016/j.physa.2012.09.014

[40] W. Xu, Z. Han, L. Tao, Q. Ding, H. Ma, Random non-convex particle model for the fraction of interfacial transition zones (ITZs) in fully-graded concrete, Powder Technol., 323 (2018) 301-309. https://doi.org/10.1016/j.powtec.2017.10.009

[41] Z. Wu, C. Shi, W. He, D. Wang. Static and dynamic compressive properties of ultra-high performance concrete (UHPC) with hybrid steel fiber reinforcements. Cem Concr Compos, 79, (2017) 148-157. https://doi.org/10.1016/j.cemconcomp.2017.02.010

[42] C. Ericson, Real-Time Collision Detection, (2004) 553–575.

[43] X. Zhou, H. Hao, Modelling of compressive behaviour of concrete-like materials at high strain rate, Int J Solids Struct, 45 (2008) 4648-4661. https://doi.org/10.1016/j.ijsolstr.2008.04.002

[44] Y. Hao, H. Hao, X. Zhang, Numerical analysis of concrete material properties at high strain rate under direct tension, Int. J. Impact Eng., 39 (2012) 51-62. https://doi.org/10.1016/j.ijimpeng.2011.08.006

[45] S. Zhang, Y. Lu, X. Chen, Influence of mesoscale three-phase parameters to the tensile behavior of concrete, Compos. Interfaces, 23 (2016) 585-605. https://doi.org/10.1080/09276440.2016.1158529

[46] Sharaddhu, Practical Grading of Aggregates | Concrete Technology, Road Research Institute UK, (2012).

[47] H. Chen, Z. Zhu, J. Lin, W. Xu, L. Liu, Numerical modeling on the influence of particle shape on ITZ's microstructure and macro-properties of cementitious composites: a critical review, Journal of Sustainable Cement-Based Materials, 7 (2018) 248-269. https://doi.org/10.1080/21650373.2018.1473818

[48] C. Qiu, Quantitative characterization and elastic properties of interfacial transition zone of concrete, Master thesis, Eastsouth University, 2012.

[49] Z. Wu, C. Shi, K. H. Khayat. Influence of silica fume content on microstructure development and bond to steel fiber in ultra-high strength cement-based materials (UHSC). Cem Concr Compos, 71 (2016) 97-109. https://doi.org/10.1016/j.cemconcomp.2016.05.005

[50] Q. Chen, H. Zhu, Z. Yan, J.W. Ju, Z. Jiang, Y. Wang, A multiphase micromechanical model for hybrid fiber reinforced concrete considering the aggregate and ITZ effects, Constr Build Mater., 114 (2016) 839-850. https://doi.org/10.1016/j.conbuildmat.2016.04.008

[51] Z. Hashin, S. Shtrikman, A variational approach to the theory of the elastic behaviour of multiphase materials ☆ , J Mech Phys Solids, 11 (1963) 127-140. https://doi.org/10.1016/0022-5096(63)90060-7

[52] Y.P. Qiu, G.J. Weng, Elastic Moduli of Thickly Coated Particle and Fiber-Reinforced Composites, J Appl Mech, 58 (1991) 388-398.

[53] A.F. Stock, D.J. Hannantt, R.I.T. Williams, The effect of aggregate concentration upon the strength and modulus of elasticity of concrete, Magazine of Concrete Research, 31.109 (1979) 225-234. https://doi.org/10.1680/macr.1979.31.109.225

[54] Z. Wu, C. Shi, W. He. Comparative study on flexural properties of ultra-high performance concrete with supplementary cementitious materials under different curing regimes. Constr Build Mater., 136 (2017) 307-313. https://doi.org/10.1016/j.conbuildmat.2017.01.052

Declaration of interests

☒ The authors declare that they have no known competing financial interests or personal relationships that could have appeared to influence the work reported in this paper.

☐The authors declare the following financial interests/personal relationships which may be considered as potential competing interests: